Available online at www.sciencedirect.com

jmr&t
Journal of Materials Research and Technology

journal homepage: www.elsevier.com/locate/jmrt

Influence of wire rolling on Zircalloy-2: tensile behaviour and microstructural investigation

Ravi Kumar Singh [a], *Sunkulp Goel* [b,c,**], *Nikhil Kumar* [a,*], *B.D.Y. Sunil* [d], *Soni Kumari* [e], *Sayed M. Eldin* [f], *Kuldeep K. Saxena* [g]

[a] *School of Materials Science and Technology, Indian Institute of Technology (BHU) Varanasi, 221005, India*
[b] *Herbert Gleiter Institute of Nanoscience, Nanjing University of Science and Technology, Nanjing, 210094, China*
[c] *Department of Mechanical Engineering, Faculty of Engineering, Teerthanker Mahaveer University Moradabad, UP, 244001, India*
[d] *Mechanical Engineering Department, Institute of Aeronautical Engineering, Hyderabad, Telangana, India*
[e] *Department of Mechanical Engineering GLA University, Mathura, India*
[f] *Center of Research, Faculty of Engineering, Future University in Egypt, New Cairo, 11835, Egypt*
[g] *Division of Research and Development, Lovely Professional University, Phagwara, 144411, India*

ARTICLE INFO

Article history:
Received 14 April 2023
Accepted 5 June 2023
Available online 8 June 2023

Keywords:
Zircalloy-2
Room temperature wire rolling
Tensile strength
EBSD
Texture
TEM

ABSTRACT

In the present work, the microstructure, tensile and texture properties of Zircalloy-2 (Zr-2) processed by the room temperature wire rolling (RTWR) have been investigated. The detail microstructural investigation was performed with the help of optical microscopy, Transmission Electron Microscopy (TEM) and Electron Back Scattered Diffraction (EBSD). Dislocation density was calculated by using X-ray diffraction (XRD) through modified Williamson Hall technique. The dislocation density increased as the true strain increased from 0.69 to 1.32, but at the same time when true strain increased from 1.32 to 2.77, dislocations density start decreasing. It was occurred due to the formation of large volume fraction of dynamic recrystallization grains (DRX) after inducing true strain of 2.77. The maximum yield strength of 750 MPa was achieved after true strain of 1.32, but as the induced true strain increased to 2.77, the yield strength decreased to 620 MPa. It was due to the formation of high volume fraction of DRX grain and grain coarsening led by the dislocations annihilation mechanism. The highest ductility was achieved after true strain of 2.77 is attributed to domination of dislocations annihilation assisted mechanism. The EBSD and tensile test investigation further confirmed the presence of Extension twinning ($\{10\bar{1}2\}<10\bar{1}1>$) after inducing a true strain of 1.32 and more, which signify the severe deformation through the RTWR. Further, deformation mechanism of Zr-2 alloy has been proposed through processing by RTWR with the help of experimental investigation.

* Corresponding author.
** Corresponding author.
E-mail addresses: sankalp20006@gmail.com (S. Goel), nikhil.mst@itbhu.ac.in, nikhil.shishodiya@gmail.com (N. Kumar).
https://doi.org/10.1016/j.jmrt.2023.06.052

1. Introduction

On the grounds of superior corrosion resistance and high strength-to-weight ratio, zirconium (Zr) alloys, such as Zircalloy-2, have seen an increase in use in nuclear reactors in recent years. However, the mechanical properties of these alloys can be further improved by various thermal and mechanical treatments [1–8]. Zr-based alloys have a lot of potential due to their extreme properties i.e. excellent corrosion resistance, transparent to thermal energy neutrons, lower neutron affinity, the form-stable phase at room temperature, and it is highly anisotropic, and have excellent yield strength [9].

Various severe plastic deformation (SPD) techniques such as equal channel angular processing, Asymmetric rolling, Multi-axial forging, High-pressure torsion, etc. had been used to increase the properties of materials [10]. Along with these SPD techniques wire rolling technique also emerged as a potential processing method. Previous works from literature about the processing of Zircalloys through the SPD route are listed in Table 1. Wire rolling of Zr-2 provided excellent yield strength of 897 MPa in our previous studies [11]. It is the most superior metal forming process for continuous fabrication of material with shapes of wires, rods etc. at a faster production rate along with minimal material waste [11]. The development of texture in the Zr-2 is the result of the material processing method and various alloying elements [12]. The crystallographic texture is an important parameter, which affects the deformation and mechanical behaviour like yield strength, ductility, formability, etc [13–15].

Literature showed that texture (0002), $(10\bar{1}0)$, $(12\bar{1}4)$, $(10\bar{1}2)$, $(10\bar{1}3)$, $(10\bar{1}1)$, $(2\bar{1}\bar{1}0)$, $(12\bar{1}4)$, $(12\bar{1}1)$ are often reported for zircalloy 2 were evolved after SPD techniques [11,18,19]. The mechanism of deformation mode during plastic deformation was identified using the evolution of texture during rolling [20]. HCP (hexagonal close-packed) metals have lower symmetry compared to FCC (face centered cubic) and BCC (Body centered cubic) metals, hence dislocations movement is more complicated in HCP metals and alloys [26]. At room temperature, Zr crystallizes in an HCP structure with an axial ratio (c/a) that is 1.593 less than the approximate ideal range of 1.633 [27]. Basal $<a>\{0002\}<11\bar{2}0>$, prismatic $<a>\{10\bar{1}0\}<11\bar{2}0>$, pyramidal $<c+a>\{10\bar{1}1\}<11\bar{2}0>$, first-order pyramidal $<c+a>\{10\bar{1}1\}<11\bar{2}3>$ and second-order pyramidal $<c+a>\{11\bar{2}2\}<11\bar{2}3>$ are active slip planes for hexagonal materials [28]. Prismatic slip is most active slip system and majorly dominate the entire plastic deformation, in the case of zirconium alloys [27]. Moreover, apart from prismatic slip, the extension twins $\{10\bar{1}2\}<10\bar{1}1>$, $\{11\bar{2}1\}<11\bar{2}6>$ and contraction twins $\{11\bar{2}2\}<11\bar{2}3>$, $\{10\bar{1}1\}<10\bar{1}2>$ also actively contribute in deformation of Zircalloy 2 [25].

The aim of this investigation is to find the influence of room temperature wire rolling on the tensile behaviour and microstructural evolution of Zircalloy-2. This will be achieved through a combination of mechanical testing and microstructural analysis using techniques such as Optical Microscopy, TEM, and Electron Back Scattered Diffraction. The findings of this investigation will provide a deeper understanding of the mechanism of room temperature wire rolling and its potential applications in the field of nuclear engineering. In the present work, different rolling reductions of 25%, 50%, and 75% are given to Zr-2 by wire rolling at room temperature and an in-depth study was performed for its microstructure development and texture evolution, including tensile tests through EBSD, TEM, and bulk texture. Dislocation density of processed samples were calculated through XRD. The Important observations made during this investigation.

- Wire Rolling emerges as an important route for the heavy deformation even at room temperature.
- First time Extension twinning $\{10\bar{1}2\}<10\bar{1}1>$ was reported after the room temperature wire rolling at true strain of 1.32.
- Novel Deformation mechanism of Zr-2 alloy Via room temperature wire rolling has been proposed with the help of experimental evidences.

2. Material and experimental methods

2.1. Sample fabrication

Zircalloy-2 rolled sheets with a 4-mm thickness were purchased from the Nuclear Fuel Complex in Hyderabad, India. The elemental composition of the as received Zr alloy is confirmed by X-ray photoelectron spectroscopy (XPS) as mentioned in Table 2. Initially, a 4×4 mm cross section billets were cut from the sheet, and then as received sample was solution treated and heated up to 800 °C in argon atmosphere and later underwent mercury quenching [9,11,22]. The Room Temperature Wire Rolling (RTWR) was performed and to ensure the room temperature, the samples were dipped in water immediately after completing each pass. The three different samples were prepared by inducing the cumulative true strain of 0.69, 1.32, and 2.77, respectively, using a laboratory rolling mill. The 110 mm roller diameter and rotational speed of 8 rpm was used during the rolling. The schematic of the discussed rolling processes is shown in Fig. 1. $MiSo_2$ was used to avoid the frictional and heat losses during the wire rolling of the alloy. Three conditions were prepared in the present investigation are denoted as; (a) 25% thickness Reduction Room Temperature Wire Rolled (RTWR-25), (b) 50% thickness Reduction Room Temperature Wire Rolled (RTWR-50), and (c) 75% thickness Reduction Room Temperature Wire Rolled (RTWR-75). The starting material was named (Mercury Quenched) MQ.

2.2. Microstructural characterization

Optical Microscopy was performed on wire-rolled zircalloy 2 samples by using a compound microscope (OM, ZEISS Axiovert 40). X-Ray Diffraction (XRD) was done through a Rigaku X-ray diffractometer to study the macrotexture with $Cu-K\alpha$ radiation of wavelength 1.54 Å and at a scanning rate of 4° per min. For all the samples, bulk texture XRD measurements were done using a PAN alytical X'Pert PRO MRD system equipment utilizing $Cu-K\alpha$ radiation. The pole figure was measured using the Standard Schulz method in reflection

Table 1 – Chemical composition, processing method, proposed mechanism/novelty, and yield strength reported in the literature.

S. No.	Composition	Processing Method	Mechanism/Study/Novelty	Yield Strength (MPa)	Application	*Reference*
1	Zircalloy 2 (1.54 Sn, 0.15 Fe, 0.12 Cr, 0.05 Ni, 0.012 O, Zr)	Cold Rolling	Two types of grains are called deforming and non-deforming grains formed after deformation. Basal orientations near non-deforming grains have most of the residual stress development.	–	Pressure tube	[16]
2	Zircalloy 2	Warm Rolling	Prismatic ⟨a⟩ slip controls the micro-yielding and $\{20\bar{2}1\}$ grains, while basal ⟨a⟩ slip has a strong impact on the yielding of pyramidal the $\{10\bar{1}1\}$, $\{10\bar{1}2\}$, $\{10\bar{1}3\}$ and $\{11\ \bar{2}\ 2\}$ grains.	450	Nuclear Industry	[17]
3	Zircalloy 2	Cast and forged	Texture generated affected the deformation mode. Twinning leads to Microstructural developments with refined grains. Deformation generates texture and in-grain misorientations.	–	Nuclear Industry	[18]
4	Zircalloy 2	Cast and forged	Origin of recrystallization texture development along with their formation around deformation bands.	–	Structural applications	[19]
5	Zircalloy 2	Warm Rolling	Texture modeling and estimation of post deformation texture. The macroscopic stress–strain responses and texture were correlated.	–	Nuclear Industry	[20]
6	Zircalloy 2	Cast and forged, cold-rolled and warm rolled.	Grain fragmentation occurs during plastic deformation as a result of dislocation realignment and recovery, as well as the development of high-angle grain-boundaries.	–	Fuel Cladding	[21]
7	Zircalloy 2	Cold Rolling	Basal plane (0002) was oriented towards 20–30° outwards in the direction normal to the rolling direction. The formation of high dislocation density, nanostructured grains, and ultra-fine grains (UFG) was responsible for increased yield strength.	679	Boiling water reactors	[22]
8	Zircalloy 2	Wire rolling at cryo temperature	Grain boundary-based deformation mechanism. Wire rolling at cryo temperature up to a strain of 2.77 results in the formation of micro shear bands and adiabatic shear bands along with UFGs and nanostructured grains leading to an increase in strength.	897	Tubing	[11]
9	Zircalloy 4	Multiaxial forging	Twinning as deformation mode. The extension twins were more favorable than the other twins seen, and their quantity grew as cumulative strain rose, as studies by EBSD measurements.	666	Nuclear Industry	[23]
10	Zircalloy 4 (Sn, Fe, Cr, Zr)	Rolling at room & Cryo temp.	Grain fragmentation and slip processes are related to deformation behavior. Higher stacking faults in the extrusion direction resulted in more dislocations accumulation and improved grain refinement.	810	Fuel Cladding	[24]
11	Zircalloy 4	Cold Rolling	Bimodal Texture formation, texture fiber spread from $<10\bar{1}0>$ to $<11\bar{2}0>$	455	Nuclear Industry	[25]

Table 2 – Chemical composition of Zircalloy 2.

Element Name	Zr	Sn	Fe & Cr	Fe
Percentage	97.5–98.2	1.2–1.7	0.2–0.3	0.1–0.2

mode [29]. Three pole figures $\{10\bar{1}0\}, \{01\bar{1}2\}$ & {0002} were measured and analyzed with the help of the MTEX module on the MATLAB platform. Determination of dislocation density, was done with the XRD data. The diffraction pattern was analyzed using PANalytical X'Pert High Score Plus software and peaks were indexed by matching the JCPDS reference pattern (00-005-0665) in the inorganic crystal structure database reported for α Zirconium. Origin 9.0 software was used to plot the graph for XRD data.

Modified Williamson Hall plot is an important method to calculate dislocation densities with the help of XRD data [30,31]. The modified Williamson–Hall plots were used to calculate dislocation density. The following reflections were taken into consideration $(10\bar{1}0)$, (0002), $(10\bar{1}1)$, $(10\bar{1}2)$ $(10\bar{2}0)$, and $(10\bar{1}3)$ reflections. The equations used are explained below [32].

$$\left\{\Delta K^2 - \left(\frac{0.9}{D^2}\right)\right\} \Big/ K^2 \cong \beta \overline{C}_{h00}\,(1 - qH^2) \tag{2}$$

where.

ΔK is the value of full-width at half-maximum (FWHM).

D is the average-grain size.

$K = (2\sin\theta)/\lambda$, θ is the diffraction-angle.

λ is the wavelength (0.154 nm for $Cu - K\alpha$.

$\beta = \pi\rho M^2 b^2/2$, ρ is the dislocation density, M is a constant depending on both the effective outer cut-off radius of dislocations and the dislocation density (approximate value is 2).

b is the magnitude of the Burgers vector.

'C_{h00}' is a constant corresponding to the elastic constants of C_{11}, C_{12}, and C_{44} based

on the elastic anisotropy expressed as- [32].

$$A_i = 2C_{44} / (C_{11} - C_{12}) \tag{3}$$

$$H^2 = \left(h^2k^2 + h^2l^2 + k^2l^2\right) \Big/ \left(h^2 + k + l^2\right) \tag{4}$$

'q' is a parameter indicating the dislocation character in the samples.

h, k, and l are Miller's indices of each peak. β was calculated form the slope of $\beta\overline{C}_{h00}\,(1 - qH^2)$ Vs ΔK^2. Similiarly q was calculated from the slope of $\left\{\Delta K^2 - \left(\frac{0.9}{D^2}\right)\right\} \Big/ K^2$ Vs H^2.

The values of C_{11}, C_{12}, and C_{44} are 1.562*10^{11}, 6.448*10^{10} and 3.565*10^{10} GPa, respectively [30].

2.2.1. TEM

Transmission Electron Microscopy (TEM) (FEI Tecnai, USA) operating at 200 kV was employed to study the microstructural features. The samples for TEM studies were prepared by polishing with emery papers from 500 to 2500 grit size till reducing the thickness of the sample to 100 nm. A punch was used to make a circular disk of 3 mm. Then twin jet polishing was done to further reduce the thickness to 20 nm. A voltage of 15 V and a temperature of −40 °C were maintained while twin jet polishing. The chemical used was a 20:80 by volume mixture of perchloric acid and methanol.

2.2.2. EBSD

The samples were polished using emery sheets from 500 to 2500 mesh size, and then cloth polishing with an alumina suspension with a mesh size of 0.24 μm was used to prepare them for EBSD. The process was repeated till obtaining the mirror-like surface finish. Then final prepared samples were undergone for the electropolishing. The chemicals used in the process were solutions containing 20 ml perchloric acid in 80 ml methanol. As Anode work piece was kept and a stainless-steel rod was used as cathode. A thin layer of the work piece was removed during the process to achieve stress-free surface. Finally, EBSD Scan (step size of 0.1 μm) was performed on the electro-polished sample at 20 kV using the FEI Quanta 300 FEG-SEM/EBSD.

For the collection and processing of EBSD data, TSL-OIM software used. Grain orientation spread (GOS) is the average of the misorientation angles to the grain mean orientation and can be calculated using EBSD data [33]. In the attempt to evaluate the GOS by TSL OIM software for a particular grain i before and after deformation the scientific equations for GOS are represented as eq. (1).

$$GOS(i) = \frac{1}{J(i)}\sum_j \omega_{ij} \tag{1}$$

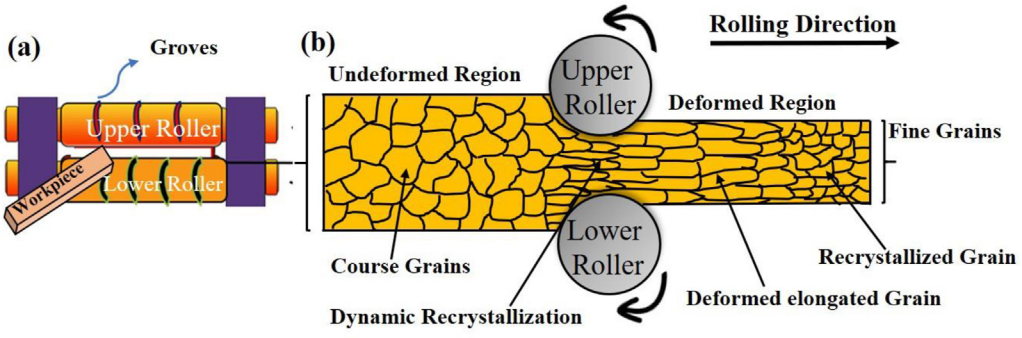

Fig. 1 – Samples prepared by wire rolling (a) Schematic of experimental setup (b)schematic of the workpiece during wire rolling process.

where $J(i)$ is the number of pixels of the grain i and ω_{ij} the misorientation angle between the orientation of pixel J and the mean orientation of grain i [34]. The dynamic recrystallized grain and deformed grains in a material are calculated using GOS [35]. Since deformed grains have very high GOS values and Recrystallized grains have low GOS values [36]. It was reported in the literature that 1°–2° is the threshold value of GOS for separating the dynamic recrystallized grains from the deformed grains [37]. In the present work, dynamic recrystallized grains and deformed grains were calculated using the criteria GOS <1° and GOS >2°, respectively, along with the condition that grain rotation angle >15°. Also, we assume low angle grain boundary to those have misorientations to be in between 2 and 15° and high angle grain boundary have misorientations greater than 15° in the experiment.

2.2.3. *Tensile test*

Tensile tests were performed on RTWR-25, RTWR-50, and RTWR-75. Dog-bone-shaped specimens of ASTM-E8-M standard were cut from Zircalloy-2 rolled samples by electric discharge machining (EDM), with gauge length parallel to the rolling direction. H25 K-S S-series tensile testing machine was used to perform the tensile-tests in a rolling direction at room temperature for 3 specimens of each type i.e. RTWR-25, RTWR-50, and RTWR-75. The tensile test was carry out on the three samples of each condition in the present work. The most representative stress–strain plot was drawn to understand the stress–strain relation. Tensile tests were performed at room temperature.

3. Results

3.1. *Optical microscopy*

Optical images of RTWR-25, RTWR-50, and RTWR-75 are showed in Fig. 2(a–c), respectively. The Grains were aligned and elongated towards the rolling direction in the RTWR-25 sample as observed in Fig. 2 (a). Wavy-type elongated grains were observed might be due to activation of multiple slip system and heterogeneous plastic flow in RTWR-50 samples as shown in Fig. 2 (b). Severely deformed grains elongated and overlapping each other were present in the RTWR-75 sample as observed in Fig. 2 (c).

3.2. *X-ray diffraction*

X-ray diffraction of RTWR-25, RTWR-50, and RTWR-75 was plotted and indexed as shown in Fig. 3. As per the XRD plot, only α-phase was present in all the samples of Zr-2 and no phase change was depicted since the temperature was not involved in the processing of Zircalloy 2. Peak shift and Peak broadening were observed in some peaks of the XRD plot demonstrated in Fig. 3 (b). Peak (0002) at 35° shifted towards a

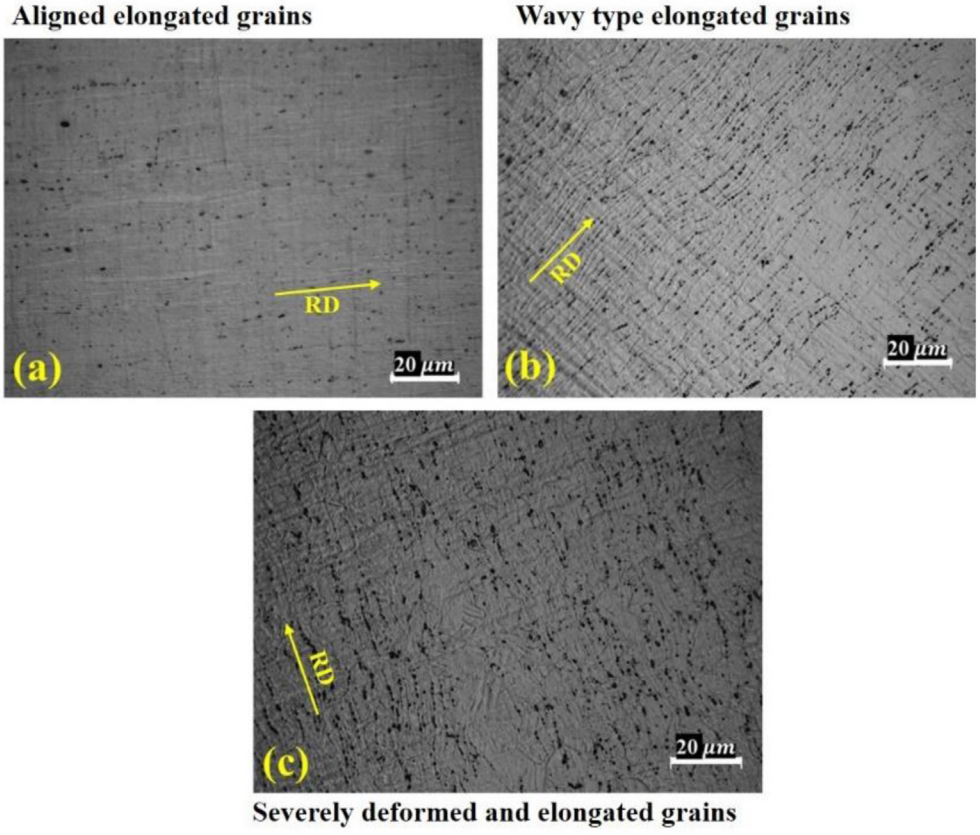

Fig. 2 – Optical Microscopy of rolled samples (a) 25% RTWR (b) RTWR-50 and (c) 75% RTWR along with rolling direction, deformed and undeformed regions.

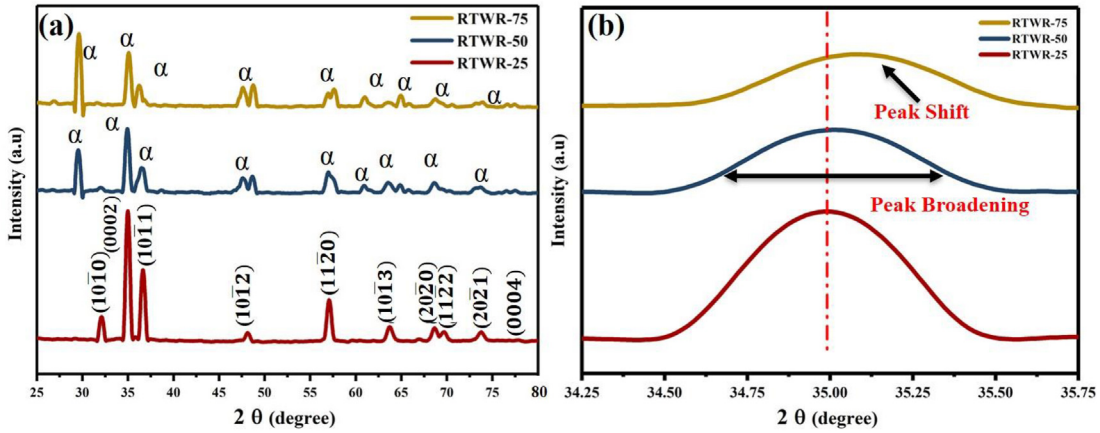

Fig. 3 – XRD data plot for Zircalloy 2 of 25% RTWR, RTWR-50 and 75% RTWR along with peak shift by (0002) plane at 34.80°.

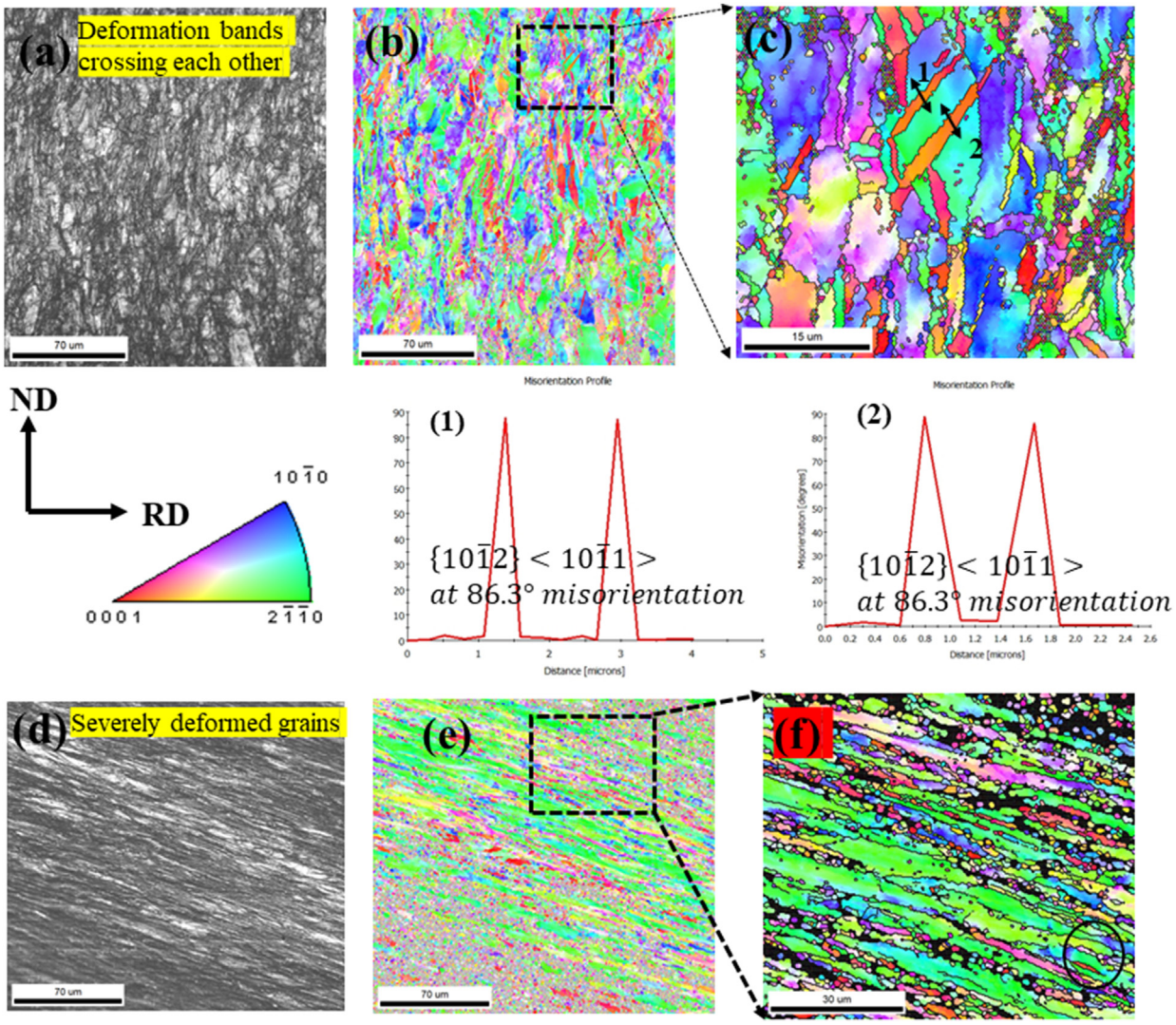

Fig. 4 – Image quality (IQ) map (a)RTWR-50 (d)RTWR-75, and Inverse pole figure (IPF) Map for (b, c) RTWR-50 (e, f) RTWR-75 Misorientation profiles for marked regions of c (1) and c (2).

higher 2^{θ} value (35.11°) for RTWR-75 because of compression in lattice and simultaneously it underwent peak broadening. Peak broadening was observed in $(10\bar{1}0)$, $(10\bar{1}2)$, $(11\bar{2}0)$, $(10\bar{1}3)$ and $(20\bar{2}0)$ for both RTWR-50 and RTWR-75.

Dislocation density was determined by applying a modified Williamson Hall plot on XRD data. Calculated dislocation density values are listed in Table 2. The abrupt behavior was noticed in the case of the RTWR-50 sample. Initially, dislocation density was increased as the rolling reduction for RTWR-50 with the increase in rolling reduction and later it decreases for further increases in the rolling reduction for RTWR-75.

3.3. EBSD

The increase in grain fragmentation can be seen with the increase in thickness reduction from RTWR-50 to RTWR-75 are shown in Fig. 4 (a, d). More elongated grains along with severe deformation were observed in RTWR-75 as compared to RTWR-50 Fig. 4a, d. Whereas, In RTWR-50 deformation bands were seen crossing each other Fig. 4a. IPF image confirms that basal plane (0001) marked in red color were present in high proportion in RTWR-50 as compared to RTWR-75. Further, magnified EBSD of RTWR-50 in Fig. 4c shows several tension twinning regions as marked in Fig. 4b. In the case of RTWR-75, Fig. 4f some marked regions showed misorientation of 86.3° showing tension twin. Misorientation profile (86.3° misoreintation) in RTWR-50, confirms the presence of extension twinning $(10\bar{1}2)<10\bar{1}1>$ [38]. The fraction of High angle grain boundaries was found to increase with RTWR reductions, as shown in Fig. 5. Evidently, with RTWR reductions dynamic recovery caused increased in the fraction of HAGB.

The total average Misorientation angle for RTWR-50 and RTWR-75 were 37.2624 ± 4, and 49.8122 ± 5, respectively (Fig. 5). From Fig. 6(a–d), dynamic recrystallization is also observed on increasing the RTWR reductions from 50% to 75%. Additionally, the deformed grains are also observed in both the conditions. Therefore, both dynamic recovery as well as recrystallization has taken place during RTWR 75% reduction.

3.4. TEM

Sub grains of size range (110 – 300) nm, (60–160) nm and (20–100) nm were formed in RTWR-25 (Fig. 7a), RTWR-50 (Fig. 7b), and RTWR-75 (Fig. 7c) respectively. TEM of RTWR-25 showed elongated grains of larger length present on the surface as compared to microstructures of RTWR-50 and RTWR-75. RTWR-75 shows a large number of fragmented grains and has ill-defined grain boundaries Fig. 7c. RTWR-75 has parallel bands inside the region highlighted in Fig. 7c confirming the formation of twins [24]. Further, highlighted region of Fig. 7c was magnified (Fig. 7d) and Selected area electron diffraction (SAED) was taken from the same region Fig. 4d, planes $(01\bar{1}2)$, (0002) and $(10\bar{1}1)$ were indexed. Discontinuous intensity distribution of rings in the SAED pattern confirmed the presence of polycrystalline material.

3.5. Macro-texture

The pole figure with poles $\{01\bar{1}2\}$, $\{10\bar{1}0\}$ and {0002} along extrusion direction in Fig. 8 (a, b, c) for RTWR-25, RTWR-50 and RTWR-75 sample were showed. Basal texture (0002) comes out to be a high-intensity texture for RTWR-25, RTWR-50, and RTWR-75. RTWR-50 and RTWR-25 had the same pattern of basal texture which was concentrated at the center but in the larger area. RTWR-75 had basal texture with a split type texture also called T-type texture [39]. In RTWR-75, the split of two peaks, one with a significant split along the TD plane and the other with a lower intensity split along the RD plane was seen with improved intensity. $(10\bar{1}0)$ texture was having two strong peaks in RTWR-25 (Fig. 8a) initially and after the increase in reduction to RTWR-50 (Fig. 8b) one strong and one weak peak

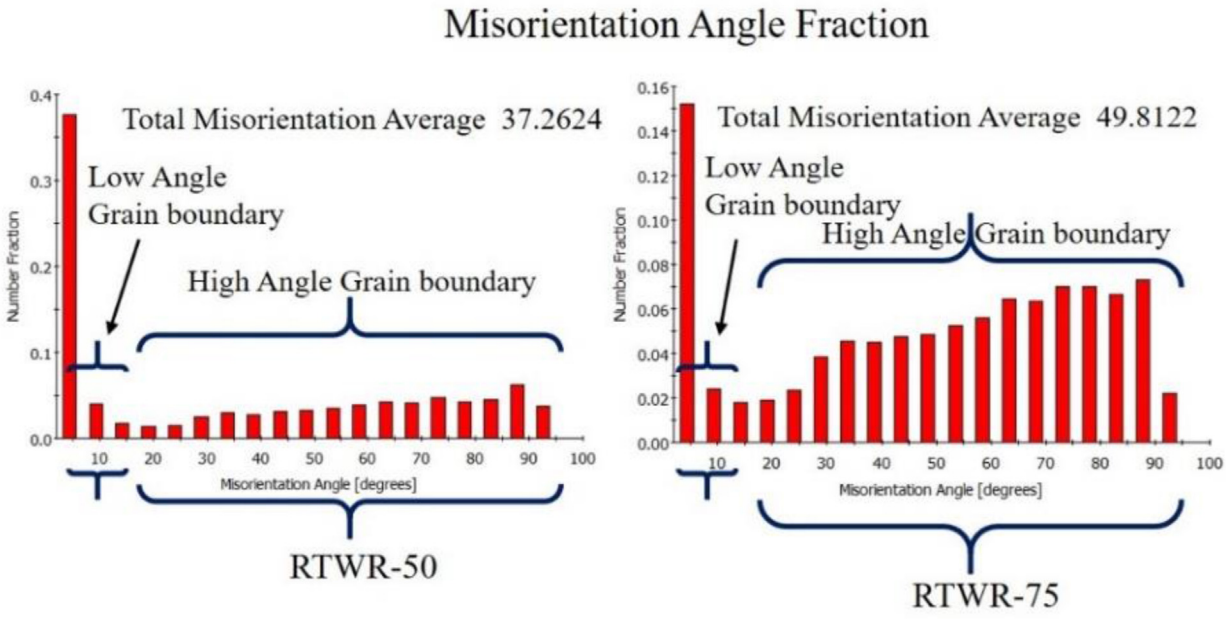

Fig. 5 – Misorientation angle Fraction for RTWR-50 and RTWR-75.

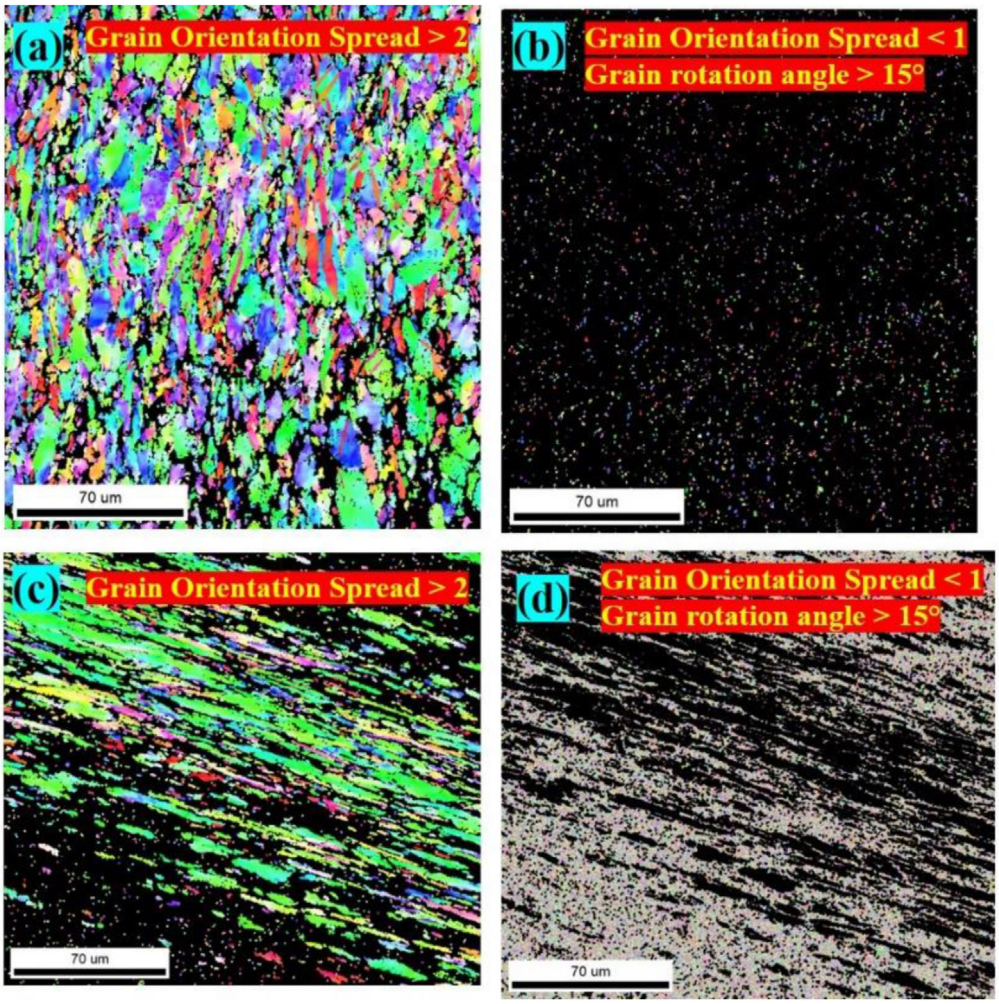

Fig. 6 – Partition of IPF to identify Deformed grain in (a)50% RTWR (b)RTWR-75 and for Recrystallized grain in (c)RTWR-50 (d) RTWR-75.

can be seen and on further reduction to RTWR-75 (Fig. 8c) texture formed in rolling direction and have one strong peak and one weak peak. $(01\bar{1}2)$ texture was having a total of three peaks, one strong and two weak peaks in RTWR-25 (Fig. 8a), two weak and one strong peak in RTWR-50 (Fig. 8b), one strong and one weak peak in RTWR-75 (Fig. 8c). Pole figure confirmed that the grains were highly oriented and in large proportion for RTWR-25 when compared to RTWR-50 and RTWR-75.

3.6. *Tensile test*

The average yield strength of RTWR-50 (750 MPa) was highest among RTWR-25 (490 MPa) and RTWR-75 (620 MPa) as shown in Fig. 9. The average Ultimate tensile strength (UTS) of RTWR-50 (880 MPa) was highest as compared to RTWR-25 (590 MPa) and RTWR-75 (820 MPa), respectively (Table 4). Ductility was highest for RTWR-75 almost 20%, and for RTWR-25 it is 7% and for RTWR-50 it is 6%. RTWR-75 was showing the formation of extension twinning along rolling direction [40,41].

4. Discussion

4.1. *Microstructure evolution*

The nature of elongated grains in optical micrographs (Fig. 2) was changed because of more strain localization as the reduction percentage increased from RTWR-25 to RTWR-75. It was also confirmed by the XRD plot as the peak of (0002) basal plane Fig. 3 (b) has shifted towards a higher value of 2 thetas, confirming the residual stresses in the material. While both RTWR-50 and RTWR-75 showed peak shift and broadening confirming lattice distortion and dislocation accumulation, respectively [42]. These imperfect lattice structures evolved due to the influences of higher stresses of Wire rolling processes. Rolling includes compression stresses and shear stresses responsible for the accumulation of strain and residual stresses on the material which leads to the formation of dislocation in the material [11]. Dislocation density calculated

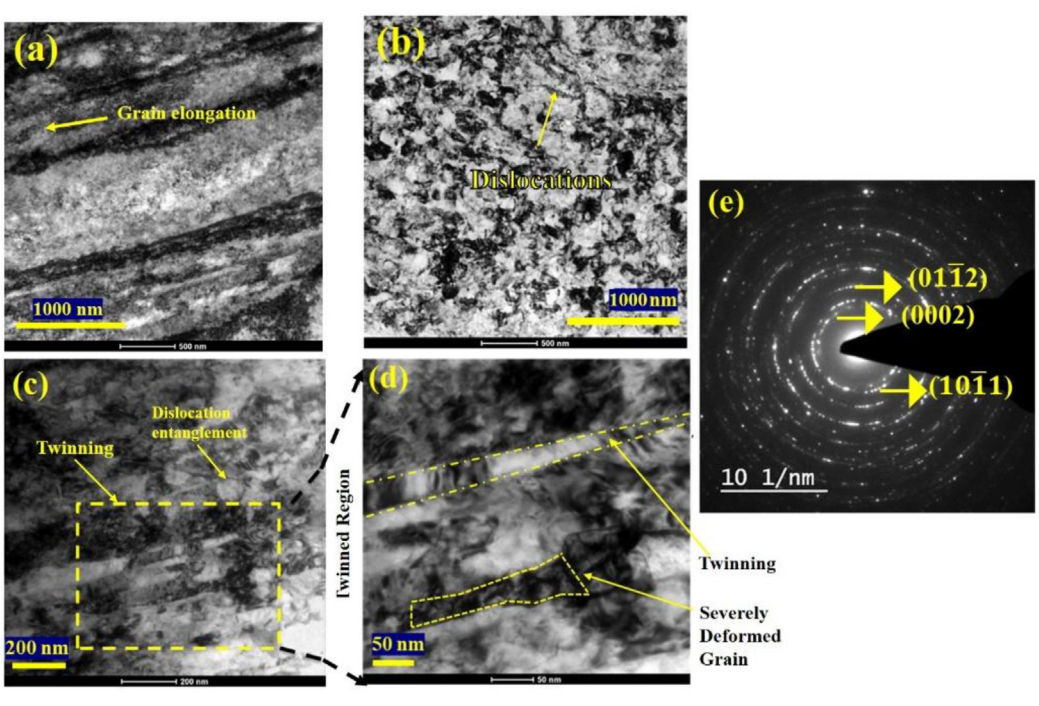

Fig. 7 – Bright field-TEM micrographs of Zircalloy 2 (a)RTWR-25, (b)RTWR-50 (c)RTWR-75 (d) magnified RTWR-75 (e) Selected area electron diffraction (SAED) pattern of RTWR-75 sample taken from 'd'.

for RTWR-25, RTWR-50 and RTWR-75 were 27.66738 * 10^{-3} nm^{-2}, 94.17962 * 10^{-3} nm^{-2} and 80.6298 * 10^{-3} nm^{-2} respectively (Table 3). Highest dislocation density for RTWR-50 condition is due to suppression of dynamic recovery up to 1.32 strain. The generation of heat during rolling and high deformation strain during RTWR-75, dislocation density decreases compared to RTWR-50. Consequently, dislocation annihilation, dynamic recrystallization (Fig. 6) and sub grain formation (Fig. 7c) started also confirmed from Fig. 6. In the microstructure of RTWR-75, several small recrystallized grains were formed as confirmed in Fig. 6 (c, d) (see Table 4).

The TEM micrographs (Fig. 7) shows the dislocations, grain boundary structure and twining. It confirms the formation of multimodal grain structure comprising both Nano and ultrafine grains (Fig. 7 a, b, c). With RTWR reduction, well defined grain boundaries are obtained with multimodal grain structure, responsible for the increase in the ductility as well as strength.

4.2. *Mechanical properties*

The microstructural evolution influenced the tensile properties significantly as can be observed from Fig. 9. The sub-grained microstructure evolved in RTWR-50 with high dislocation density provides the inductive platform for dislocations annihilation and dynamic recrystallization further up to RTWR-75 (Fig. 6 (c, d)). Due to the recovery effect, the dislocation density in the RTWR-50 has a limit to increase furthermore as calculated in Table 3. The presence of high dislocation density causes the maximum increase in the yield strength (750 MPa) for RTWR-50 sample when compared to other samples (Table-4). The mechanism behind the maximum yield strength of RTWR-50 was grain boundary strengthening [43]. It was important to notice that at the early stage of rolling i.e true strain 0.69 dislocations entanglement was not seen but as the true strain in material increased beyond 0.69, the dislocations entanglement was found Fig. 7 (a, b, c). When true strain increased to 2.77 (RTWR-75), the recrystallization was dominated and further act as a driving force for reducing the strength. This was due to a large amount of plastic deformation accumulation during RTWR-75 at deformation bands and at grain boundaries. This accumulated deformation act as driving force for the nucleation of stress free new grains at the deformation bands and grain boundaries, further leading to development of fully developed dynamic recrystallized grains. That was the major reason for decrease in yield strength (620 MPa) and increase in ductility (≈21 %) of RTWR-75. Here, the RTWR-75 was showing the maximum ductility as compared to other investigated samples. This was due to the role of dynamic recrystallization. During dynamic recrystallization formation of new grains can cause the original grains to shrink in size, resulting in a more uniform distribution of strain within the material. This, in turn, improving the Zircaloy-2 ductility by reducing the possibility of localized strain concentrations and promoting more homogeneous deformation.

4.3. *Deformation mechanism*

The deformation mechanism in RTWR Zr-2 has two stages of deformation, one at lower strains and another at higher strains. At lower strains (true strain 0.69) in RTWR-25, partially

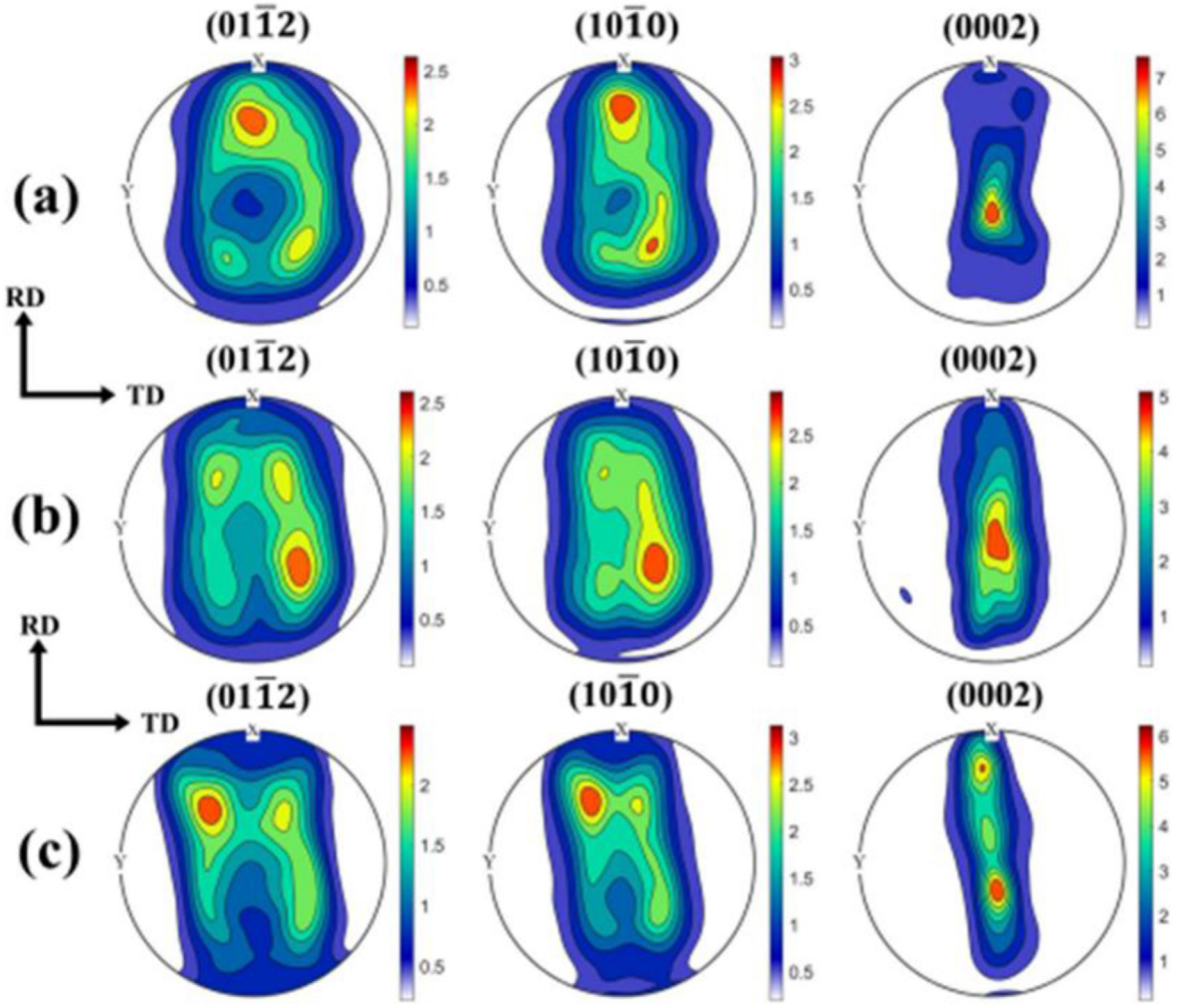

Fig. 8 – Pole Figure {01$\bar{1}$2}, {10$\bar{1}$0} and {0002} for (a)RTWR-25 (b)RTWR-50 and (c)RTWR-75.

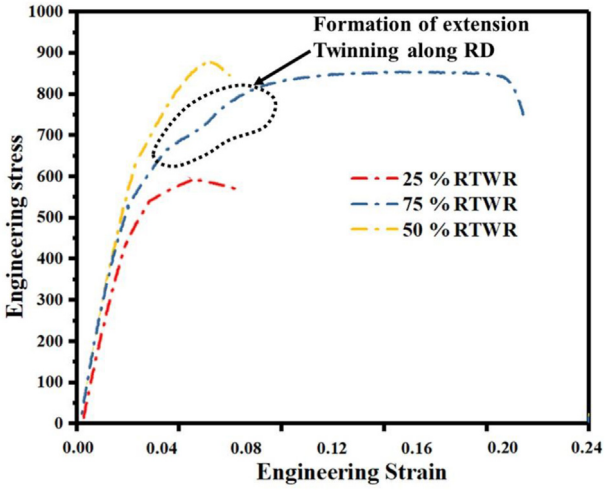

Fig. 9 – Engineering Stress –Engineering strain curve for RTWR-25 RTWR-50 and RTWR-75 samples.

Table 3 – Calculated Dislocation density with Modified Williamson Hall plot.

	Dislocation Density (δ) $\delta * 10^{-3}$ nm^{-2} (or 10^{15} m^{-2})
Zircalloy 2 (a) 25% RTWR	27.66738
Zircalloy 2 (b) 50% RTWR	94.17962
Zircalloy 2 (c) 75% RTWR	80.6298

Table 4 – The average Yield strength and UTS with standard deviation of RTWR-25, RTWR-50, RTWR-75 and MQ.

Sample	Yield Strength (MPa)	UTS (MPa)
MQ	390 ± 22	490 ± 21
RTWR-25	490 ± 23	590 ± 25
RTWR-50	750 ± 19	880 ± 16
RTWR-75	620 ± 20	820 ± 17

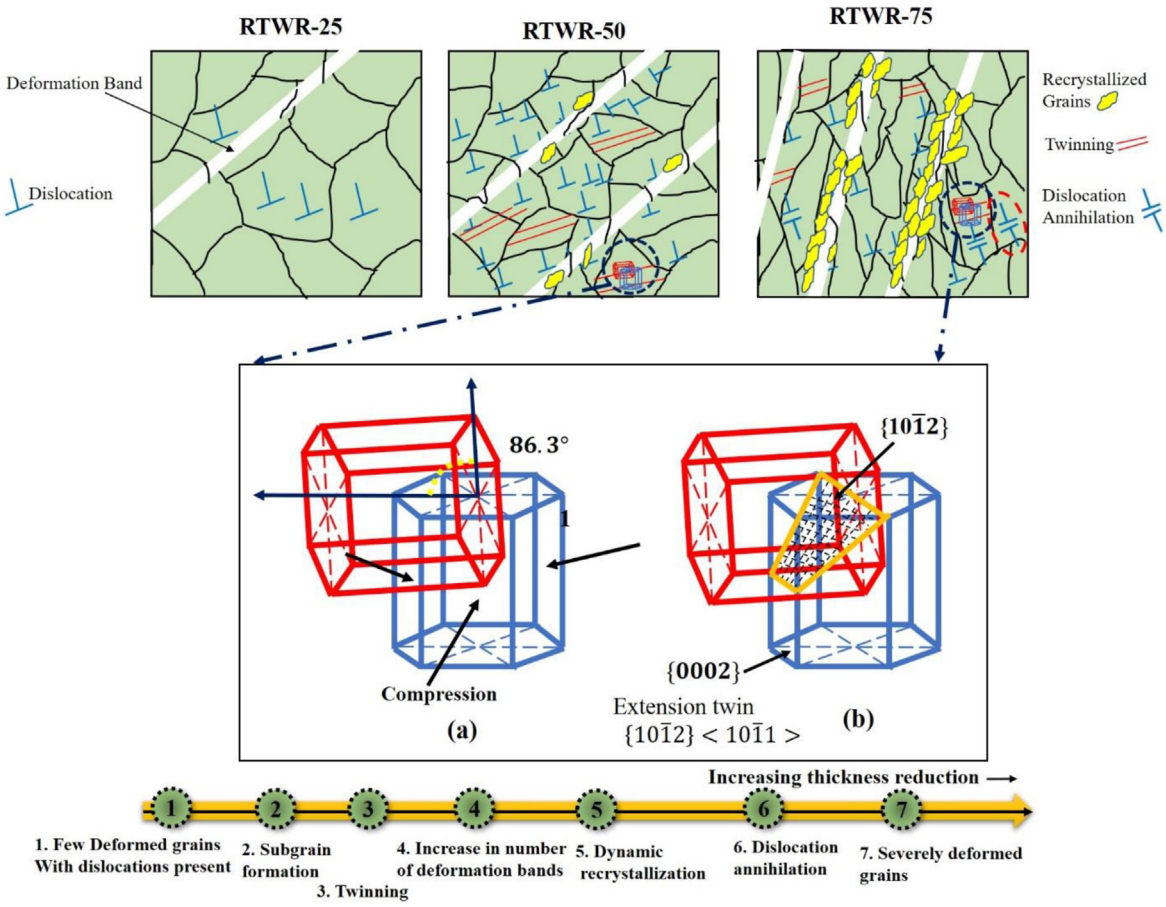

Fig. 10 – Microstructure behaviour along with {10$\bar{1}$2} <10 $\bar{1}$ 1> extension twinning formation because of compression (a) angle between two twinned crystal (b)Twinning plane.

deformed grains (Fig. 7a) are generated in such a manner that dislocations arise from the boundaries of deformed grains. With the increase in further true strain of 1.32, some deformation twins became active in the material as evident from Fig. 4c. Simultaneously, the dislocations build up in dislocation walls, causing their misorientations to increase until they become high-angle grain boundaries. Dislocations mobilized without much grain boundary hindrance, as high angle grain boundaries (HAGBs) were not evolved mostly as per the EBSD observations Fig. 5. Rather, there are low angle grain boundaries (LAGBs) that are evolved due to progressive rotation of localized regions in the existing grain misorientations, and hence several sub grains are grown while deformation. At higher strains (beyond true strain 1.32), grains become severely deformed, and parallel a softening mechanism because of dislocations annihilation and nucleation of dynamic recrystallized grains started, nearby the deformed grain boundaries and as well as at deformation bands (Fig. 10).

Despite the presence of extension twin in RTWR-75, the ductility was improved because the proportion of these twin system was around 7% only (Fig. 5), also explained in previous section. Here, the twinning system present was {10$\bar{1}$2}< 10$\bar{1}$1> called extension twinning confirmed by EBSD plot Fig. 4c. The misorientation is found to be 86.3° confirms the case of extension twin presence [11,38]. The parent grain's c-axis is parallel to the loading direction, allowing for c-axis extension and extension twin formation. During extension twinning lattices are aligned at 86.3° on their c-axis, also demonstrated in Fig. 10. A common plane {10$\bar{1}$2} is available for further dislocation movement also called twinning plane in the direction of <11$\bar{2}$0>. This type of twinning system is responsible for the increase in Taylor factor and it further make it difficult to deform the material [44]. But simultaneously recrystallization of grains was reducing its yield strength. In summary, a proper schematic is shown in Fig. 10 to explain the deformation behavior of Zr-2. It was concluded that RTWR-75 (as the true strain increasing) had a combined effect of dislocations interaction, twining and dynamic recrystallization on its deformation behavior as well as on its properties.

5. Conclusions

In the present study, Zircaloy-2 was processed through RTWR route to prepare three samples of true strain 0.69, 1.32 and 2.77. Microstructure, texture evolution and tensile properties during the RTWR was investigated. The results are summarized as follows.

- Strong Texture $\{10\bar{1}0\}$, $\{01\bar{1}2\}$ and {0002} was present along RD in RTWR-25, RTWR-50, and RTWR-75. Although, basal texture (0002) had the highest peak intensity present. Formation of basal texture to large extent supports non-homogeneous deformation of grains. The basal texture was large in volume in RTWR-25 but as rolling reduction increases the intensity of basal texture got reduced in RTWR-75.
- Excessive rolling reduction leads to Non-homogeneous deformation (in RTWR-25) of grains to homogeneous deformation of grains (RTWR-75). As the strain increases more grain fragmentation was observed leading to the development of sub grains of size range (110–300) nm, (60–160) nm, (20–100) nm in RTWR-25, RTWR-50 and RTWR-75 respectively. Dynamic Recrystallization was observed quantitatively in more domain sizes for RTWR-75 samples.
- Yield strength observed for RTWR-25, RTWR-50, and RTWR-75 were 490 ± 23 MPa, 750 ± 19 MPa, and 620 ± 20 MPa respectively. Excellent ductility was observed for RTWR-75 approximately 21%, and for RTWR-25 it was 7% and for RTWR-50 it was 6%. Initially, at a lower reduction, fine grains increase yield strength for RTWR-50 according to the grain boundary strengthening mechanism, but on further increase in rolling reduction dynamic recrystallization and dislocations annihilation acted as softening mechanism to increase ductility for RTWR-75.
- Extension twinning $\{10\bar{1}2\}<12\bar{1}0>$ was present in RTWR-50 and RTWR-75.
- Dislocation density observed for RTWR-25, RTWR-50 and RTWR-75 were 27.66738 * 10^{-3} nm^{-2}, 94.17962 * 10^{-3} nm^{-2} and 80.6298 * 10^{-3} nm^{-2} respectively.

This work gives an outstanding and deep study on zircalloy-2 at room temperature wire rolling. It will help in material design for particular room temperature applications in nuclear industries and structural applications. Zricalloy-2 alloys have the potential to be part of nuclear technology. This work was limited to experimental studies; real-time simulations would also be studied in the future.

Data availability

The raw/processed data required to reproduce these findings cannot be shared at this time as the data also forms part of an ongoing study.

Declaration of Competing Interest

The authors declare the following financial interests/personal relationships which may be considered as potential competing interests: Dr. Nikhil Kumar reports financial support was provided by Science and Engineering Research Board.

Acknowledgement

The authors acknowledge the financial support from grant SERB-SRG/2022/000978.

REFERENCES

[1] Degueldre C, Raabe J, Kuri G, Abolhassani S. Zircaloy-2 secondary phase precipitate analysis by X-ray microspectroscopy. Talanta 2008;75:402–6. https://doi.org/10.1016/J.TALANTA.2007.11.052.

[2] Kaliaraj GS, Thukkaram S, Alagarsamy K, Kirubaharan AMK, Paul LK, Abraham L, et al. Silver-calcia stabilized zirconia nanocomposite coated medical grade stainless steel as potential bioimplants. Surface Interfac 2021;24. https://doi.org/10.1016/j.surfin.2021.101086.

[3] Kaliaraj GS, Muthaiah B, Alagarsamy K, Vishwakarma V, Kirubaharan AMK. Role of bovine serum albumin in the degradation of zirconia and its allotropes coated 316L SS for potential bioimplants. Mater Chem Phys 2021;258. https://doi.org/10.1016/j.matchemphys.2020.123859.

[4] Hwang GS, In WK, Lee CY. Quenching experiments of vertical Inconel and Zircaloy tubes in internal water flow. Ann Nucl Energy 2022;167:108798. https://doi.org/10.1016/J.ANUCENE.2021.108798.

[5] Colldeweih AW, Fagnoni F, Trtik P, Zubler R, Pouchon MA, Bertsch J. Delayed hydride cracking in Zircaloy-2 with and without liner at various temperatures investigated by high-resolution neutron radiography. J Nucl Mater 2022;561:153549. https://doi.org/10.1016/J.JNUCMAT.2022.153549.

[6] Li Q, Wang Y, Du P, Song P, Zhang R, Li Z, et al. Oxidation properties and microstructure of a chromium coating on zircaloy-4 fuel cladding material applied by atmospheric plasma spraying. J Nucl Mater 2022;560:153496. https://doi.org/10.1016/J.JNUCMAT.2021.153496.

[7] Kane KA, Lee SK, Bell SB, Brown NR, Pint BA. Burst behavior of nuclear grade FeCrAl and Zircaloy-2 fuel cladding under simulated cyclic dryout conditions. J Nucl Mater 2020;539:152256. https://doi.org/10.1016/J.JNUCMAT.2020.152256.

[8] Duarte LI, Fagnoni F, Zubler R, Gong W, Trtik P, Bertsch J. Effect of the inner liner on the hydrogen distribution of zircaloy-2 nuclear fuel claddings. J Nucl Mater 2021;557:153284. https://doi.org/10.1016/J.JNUCMAT.2021.153284.

[9] Goel S, Keskar N, Jayaganthan R, Singh Iv, Srivastava D, Dey GK, et al. Mechanical behaviour and microstructural characterizations of ultrafine grained Zircaloy-2 processed by cryorolling. Materials Science and Engineering: A 2014;603:23–9. https://doi.org/10.1016/J.MSEA.2014.02.025.

[10] Estrin Y, Vinogradov A. Extreme grain refinement by severe plastic deformation: a wealth of challenging science. Acta Mater 2013;61:782–817. https://doi.org/10.1016/J.ACTAMAT.2012.10.038.

[11] Goel S, Kumar N, Jayaganthan R, Singh Iv, Srivastava D. Role of shear localization in nanocrystallisation of zircaloy-2 processed by wire rolling at cryo temperature. Mater Sci Eng: A 2018;718:111–22. https://doi.org/10.1016/J.MSEA.2018.01.089.

[12] Cheadle BA, Ells CE, Evans W. The development of texture in zirconium alloy tubes. J Nucl Mater 1967;23:199–208. https://doi.org/10.1016/0022-3115(67)90065-7.

[13] Cui C, He J, Wang W, Chen W, Zhang W. Microstructure, texture and mechanical properties of extruded AZ31 Mg alloy during small strain multi-directional forging with gradient cooling. J Alloys Compd 2022;909:164795. https://doi.org/10.1016/J.JALLCOM.2022.164795.

[14] Bache MR, Evans WJ. Impact of texture on mechanical properties in an advanced titanium alloy. Mater Sci Eng: A 2001;319–321:409–14. https://doi.org/10.1016/S0921-5093(00)02034-7.

[15] Wang L, Zhou P, Hu Y, Wang B. Effect of microstructure and texture on the mechanical properties in high strength pipeline bend. Int J Pres Ves Pip 2022;195:104604. https://doi.org/10.1016/J.IJPVP.2021.104604.
[16] Sahoo SK, Hiwarkar VD, Samajdar I, Dey GK, Srivastav D, Tiwari R, et al. Heterogeneous deformation in single-phase Zircaloy 2. Scr Mater 2007;56:963–6. https://doi.org/10.1016/J.SCRIPTAMAT.2007.02.008.
[17] Xu F, Holt RA, Daymond MR. Modeling lattice strain evolution during uniaxial deformation of textured Zircaloy-2. Acta Mater 2008;56:3672–87. https://doi.org/10.1016/J.ACTAMAT.2008.04.019.
[18] Sahoo SK, Hiwarkar VD, Majumdar A, Samajdar I, Pant P, Dey GK, et al. Presence and absence of significant twinning: effects on cold deformed microstructures of single phase Zircaloy 2. Mater Sci Eng: A 2009;518:47–55. https://doi.org/10.1016/J.MSEA.2009.05.025.
[19] Vanitha C, Kiran Kumar M, Dey GK, Srivastava D, Tewari R, Banerjee S. Recrystallization texture development in single-phase Zircaloy 2. Mater Sci Eng: A 2009;519:51–60. https://doi.org/10.1016/J.MSEA.2009.04.042.
[20] Xu F, Holt RA, Daymond MR. Modeling texture evolution during uni-axial deformation of Zircaloy-2. J Nucl Mater 2009;394:9–19. https://doi.org/10.1016/J.JNUCMAT.2009.07.006.
[21] Sahoo SK, Hiwarkar VD, Mani Krishna Kv, Samajdar I, Pant P, Pujari PK, et al. Grain fragmentation and twinning in deformed Zircaloy 2: response to positron lifetime measurements. Mater Sci Eng: A 2010;527:1427–35. https://doi.org/10.1016/J.MSEA.2009.10.066.
[22] Goel S, Jayaganthan R, Singh Iv, Srivastava D, Dey GK, Saibaba N. Mechanical and microstructural characterizations of ultrafine grained Zircaloy-2 produced by room temperature rolling. Mater Des 2014;55:612–8. https://doi.org/10.1016/J.MATDES.2013.09.039.
[23] Fuloria D, Nageswararao P, Jayaganthan R, Jha S, Srivastava D. An investigation of deformed microstructure and mechanical properties of Zircaloy-4 processed through multiaxial forging. Mater Chem Phys 2016;173:12–25. https://doi.org/10.1016/J.MATCHEMPHYS.2015.09.025.
[24] Fuloria D, Kumar N, Goel S, Jayaganthan R, Jha S, Srivastava D. Tensile properties and microstructural evolution of Zircaloy-4 processed through rolling at different temperatures. Mater Des 2016;103:40–51. https://doi.org/10.1016/J.MATDES.2016.04.052.
[25] Guo W, Li G, Yuan F, Han F, Zhang Y, Ali M, et al. Texture development and mechanical behavior of Zircaloy-4 alloy plates fabricated by cold rolling and annealing. Mater Sci Eng: A 2021;807:140846. https://doi.org/10.1016/J.MSEA.2021.140846.
[26] Goel S, Jayaganthan R, Singh Iv, Srivastava D, Dey GK, Saibaba N. Texture evolution and ultrafine grain formation in cross-cryo-rolled zircaloy-2. Acta Metall Sin 2015;28:837–46. https://doi.org/10.1007/s40195-015-0267-z.
[27] Xu F, Holt RA, Daymond MR. Evidence for basal ⟨a⟩-slip in Zircaloy-2 at room temperature from polycrystalline modeling. J Nucl Mater 2008;373:217–25. https://doi.org/10.1016/J.JNUCMAT.2007.05.052.
[28] Murty KL, Charit I. Texture development and anisotropic deformation of zircaloys. Prog Nucl Energy 2006;48:325–59. https://doi.org/10.1016/J.PNUCENE.2005.09.011.
[29] Cullity BD. Elements of X-ray diffraction. Addison-Wesley Publishing; 1956.
[30] Kishor R, Sahu L, Dutta K, Mondal AK. Assessment of dislocation density in asymmetrically cyclic loaded non-conventional stainless steel using X-ray diffraction profile analysis. Mater Sci Eng 2014;598:299–303. https://doi.org/10.1016/j.msea.2014.01.043.
[31] das Bakshi S, Sinha D, Ghosh Chowdhury S. Anisotropic broadening of XRD peaks of α'-Fe: Williamson-Hall and Warren-Averbach analysis using full width at half maximum (FWHM) and integral breadth (IB). Mater Charact 2018;142:144–53. https://doi.org/10.1016/J.MATCHAR.2018.05.018.
[32] Naghizadeh M, Mirzadeh H. Processing of fine grained AISI 304L austenitic stainless steel by cold rolling and high-temperature short-term annealing. Mater Res Express 2018;5. https://doi.org/10.1088/2053-1591/aac461.
[33] Li Z, Xie H, Jia F, Lu Y, Yuan X, Jiao S, et al. Study on deformation characteristics and microstructure evolution of 2205/ah36 bimetal composite in a novel hot forming process. Metals 2020;10:1–17. https://doi.org/10.3390/met10101375.
[34] Allain-Bonasso N, Wagner F, Berbenni S, Field DP. A study of the heterogeneity of plastic deformation in IF steel by EBSD. Mater Sci Eng: A 2012;548:56–63. https://doi.org/10.1016/J.MSEA.2012.03.068.
[35] Kumar N, Jayaganthan R, Owolabi GM. Grain refinement mechanism in 6082 Al alloy fabricated by cryo-multiaxial forging. Mater Sci Eng: A 2022;833:142518. https://doi.org/10.1016/J.MSEA.2021.142518.
[36] Kumar N. An exploration of microstructural in-homogeneity in the 6082 Al alloy processed through room temperature multi-axial forging. Mater Charact 2021;176:111134. https://doi.org/10.1016/J.MATCHAR.2021.111134.
[37] Prithiv TS, Bhuyan P, Pradhan SK, Subramanya Sarma V, Mandal S. A critical evaluation on efficacy of recrystallization vs. strain induced boundary migration in achieving grain boundary engineered microstructure in a Ni-base superalloy. Acta Mater 2018;146:187–201. https://doi.org/10.1016/j.actamat.2017.12.045.
[38] Lentz M, Risse M, Schaefer N, Reimers W, Beyerlein IJ. Strength and ductility with {10 11}-{1012} double twinning in a magnesium alloy. Nat Commun 2016;7. https://doi.org/10.1038/ncomms11068.
[39] Fuloria D, Kumar N, Jayaganthan R, Jha SK, Srivastava D. Microstructural and textural characterization of Zircaloy-4 processed by rolling at different temperatures. Mater Charact 2017;127:296–310. https://doi.org/10.1016/J.MATCHAR.2017.02.020.
[40] Barnett MR. Twinning and the ductility of magnesium alloys: Part I: "Tension" twins. Materials Science and Engineering: A 2007;464:1–7. https://doi.org/10.1016/J.MSEA.2006.12.037.
[41] Chen P, Li B, Culbertson D, Jiang Y. Contribution of extension twinning to plastic strain at low stress stage deformation of a Mg-3Al-1Zn alloy. Mater Sci Eng 2018;709:40–5. https://doi.org/10.1016/j.msea.2017.10.038.
[42] Farkas G, Groma I, Veselý J, Máthis K. Evaluation of X-ray Bragg peak profiles with the variance method obtained by in situ measurement on Mg–Al alloys. J Appl Crystallogr 2020;53:360–8. https://doi.org/10.1107/S1600576720000709.
[43] Peterson A, Baker I. Analysis of the elevated temperature deformation mechanisms and grain boundary strengthening of the alumina-forming austenitic stainless steel Fe–20Cr–30Ni–2Nb–5Al. Mater Sci Eng: A 2021;814:141219. https://doi.org/10.1016/J.MSEA.2021.141219.
[44] Tsukamoto G, Kunieda T, Mitsuhara M, Nakashima H. Effect of twinning deformation on work hardening in commercially pure titanium. Mater Sci Eng: A 2022;840:142907. https://doi.org/10.1016/J.MSEA.2022.142907.